Direct observation of pressure-induced amorphization of methane/ethane hydrates using Raman and infrared spectroscopy

Naoki Noguchi,*[a] Yui Shiraishi,[a] Maho Kageyama,[a] Yuu Yokoi,[a] Saki Kurohama,[a] Natsuki Okada [a] and Hidekazu Okamura [a]

Abstract

The pressure-induced amorphization (PIA) of ice and clathrate hydrates occurs at temperatures significantly below their melting and decomposition points. The PIA of type I clathrate hydrates containing methane and ethane as guest molecules was investigated using Raman and infrared (IR) spectroscopy. With isothermal compression at 100 K, methane hydrate (MH) underwent PIA at 2–3.5 GPa, whereas ethane hydrate (EH) underwent PIA at 4.0–5.5 GPa. The type I clathrate structure consists of small (5^{12}) and large ($5^{12}6^2$) cages. The Raman results revealed that the collapsed small and large cages in the amorphous forms of MH and EH were not distinguishable. The collapsed cages, including the methane and ethane molecules, were similar to the small and large cages, respectively. Their water networks were folded or expanded during the PIA process so that the cavity sizes of the collapsed cages were compatible with those of the guest molecules. Peaks in the IR spectra of crystalline MH assignable to the ro-vibrational transition of methane in large cages were observed in the C-H stretching wavenumber region below 40 K. The ro-vibrational IR band disappeared after amorphization, suggesting that the rotational motion of the methane molecule in the large cage was frozen by the collapse, as reported in previous dielectric spectroscopic and simulation studies. This study contributes to a better understanding of the changes in the local structure around guest molecules during PIA and the dynamics of the guest molecules.

[a] *Graduate School of Technology, Industrial and Social Sciences, Tokushima University, 2-1 Minami-josanjima-cho, Tokushima 770-8506, Japan*

E-mail: noguchi.naoki@tokushima-u.ac.jp;

Tel.: +81-88-656-9977;

Fax: +81-0858-43-2184

Introduction

The "two-liquid hypothesis of water" is very attractive, but it is a controversial topic even in current studies.[1] The cornerstone of the hypothesis is "polyamorphs" of ice.[2] At least three distinct forms of amorphous ice exist, namely, low-density amorphous (LDA), high-density amorphous (HDA),[3,4] and very high-density amorphous (VHDA).[5] X-ray and neutron diffraction studies have shown distinct differences in the structure of the amorphous forms.[6,7] They pointed out the structural similarities between ice I_h and LDA, that between liquid water at room temperature and HDA. HDA is obtained via the pressure-induced amorphization (PIA) of ice I_h, which occurs around 1 GPa below 130 K.[3] On the other hand, LDA is formed when HDA recovered at ambient pressure and low temperatures is heated at 120–140 K.[4] The clathrate hydrates, whose host structure consists of a hydrogen-bonded water network similar to ice, collapse to an amorphous form upon isothermal compression at low temperatures. The similarity in their preparation routes suggests that the structure of the amorphous clathrate hydrate is analogous to that of HDA.

The PIA of clathrate hydrates was first reported in a study on tetrahydrofuran (THF) and SF_6 hydrates, which have a type II clathrate structure.[8–10] Thereafter, PIA was observed in various type II clathrate hydrates containing 1,3-dioxolane, cyclobutanone, and noble gas elements as guest molecules or atoms.[11–13] Tulk *et al.*[14] reported that methane hydrate (MH), which has a type I clathrate structure, undergoes PIA at 3.2 GPa under isothermal compression at 100 K. The unit cell of type I clathrate hydrates is composed of two small cages and six large cages (**Fig. S1**). Both cages can contain one guest methane or ethane molecule, although the actual MH or ethane hydrate (EH) crystals also contain vacant cages.

A comparison between the PIAs of ice and clathrate hydrates is important for elucidating the mechanism of the PIA of ice. Representative similarities between both the amorphization processes and forms are (i) the PIAs occur on the isothermal compression at low temperatures significantly below their melting and decomposition points,[3,14,15] (ii) the amorphous forms are densified and relaxed by annealing,[16–19] and (iii) glass transition occurs by annealing.[11,12,15,19,20] In contrast, representative differences are (i) changes in the thermal conductivity during amorphization,[11,12,17] and (ii) the recrystallization temperatures of amorphous clathrate hydrates after annealing are higher than those of amorphous ice.[11,12,14] The structure and the dynamics of the guest molecules in the amorphous type I and II clathrate hydrates are key to interpreting the origin of the differences. In the neutron diffraction patterns of the amorphized clathrate hydrates, the first diffraction peaks (FDPs) are split,[14,16,21] whereas those of the three amorphous ices are unsplit.[6,7] Furthermore, annealing the amorphous clathrate hydrates at 130–170 K aggregates their split FDP into a single peak and slightly shifts the peak position toward higher energies for increasing momentum transfers, which means that the structure is densified.[14,16,21] The diffraction patterns of the amorphous clathrate hydrates simulated using molecular dynamics (MD) simulations suggested that the split FDP is due to the cavity structure provided by the guest-water repulsion.[13,14,18,21,22] Furthermore, they suggested that the local water structures of the amorphous clathrate hydrates after annealing are similar to those of amorphous ices. However, the water network and detailed

local environment around the guest molecules in amorphous clathrate hydrates before and after annealing remain unclear.

Vibrational spectroscopy is useful for elucidating guest molecule dynamics and local structures around the guest molecules. Vibron stretching frequencies of the guest molecules reflect the host-guest interaction according to the "loose cage-tight cage" model in the crystalline and amorphous states.[23,24] Weakening the interaction by increasing the host-guest distance induces the negative frequency shifts of the stretching modes, namely, "the larger the cavity, the lower the frequency."[23] In particular, the symmetric CH stretching (ν_1) mode of methane molecules and the CC stretching (ν_3) mode of ethane molecules (**Fig. S2**) are good environmental indicators of the guest molecules because they are non-degenerate. That is, their modes cannot be split depending on the symmetry of the crystal field around the guest molecules. Furthermore, in the infrared (IR) spectra of MH below 40 K, bands assigned to the ro-vibrational transition appeared in the wavenumber region of the asymmetric stretching (ν_3) mode of the methane molecules in the large cages (**Fig. S2**).[25,26] This is evidence of the quasi-rotor behavior of methane molecules. Therefore, the rotational dynamics of the guest methane molecule in MH can be investigated using the IR spectra at low temperatures.

Raman and IR spectra of MH and EH were acquired at temperatures and pressures of 8–295 K and 0.1–8 GPa, respectively, and the PIAs of MH and EH as well as the annealing effect on their amorphous forms were investigated. To the best of our knowledge, this is the first study of the PIA of EH. A comparison of the spectra of both amorphized hydrates allowed us to gain insight into the effect of the size of the guest molecules on the collapse process and their amorphous forms. The cavity radii of the small and large cages in the type I clathrate structure are approximately 3.9 and 4.3 Å, respectively, whereas the van der Waals radii of the methane and ethane molecules are 2.2 and 2.8 Å, respectively.[27] The host-guest repulsive interaction in EH undoubtedly has a greater influence on the structural evolution during PIA than in MH. The structural differences between amorphous MH and EH, as well as the rotational dynamics of the methane molecules in MH, are discussed based on the Raman and IR spectra.

Experimental Methods

Syntheses of MH and EH

To avoid wavenumber overlap between the OH and CH stretching modes, MH and EH samples whose host cages were composed of D_2O were used. Commercial D_2O (99.9% purity) was used as the starting material. D_2O and a magnetic stirrer bar were placed in a high-pressure gas reactor that was pressurized with CH_4 and C_2H_6 gases to 9 and 4 MPa, respectively. The reactor was then placed in a temperature-controlled cooling bath. The materials were held at 278–279 K for 12–24 h, cooled, and then held at 259–266 K for 24–48 h. A magnetic stirrer was used to promote the reaction between the liquid D_2O and the CH_4 or C_2H_6 gases. The products were identified as MH and EH type I clathrates using Raman spectroscopy.

High-pressure experiments

A diamond anvil cell (DAC) made of CuBe alloy was used to generate high pressures. A He-gas membrane was used as the force generation system. The DAC was equipped with a pair of type Ia diamond anvils with a 600 or 800-μm diameter culet. An approximately 100 μm-thick pre-indented SUS 301 foil with a 300 μm-diameter hole was used as the gasket. The powdered D_2O-substituted MH or EH and a CaF_2 plate were loaded into the sample hole with two or three ruby chips for pressure measurement in a freezer,[28] followed by pressurization of the DAC to 0.2–1 GPa below 240 K. The CaF_2 plate, which was transparent in the mid-IR region, acted as a filler, preventing saturation of the IR absorption of the sample by reducing the optical path length of the IR light. No pressure medium was used. The MH and EH phases loaded in the DAC were identified using micro-Raman spectroscopy. A small amount of H_2O originating from ambient air was also mixed into the sample. The DAC was attached to a liquid He/N_2 continuous flow cryostat for low-temperature measurements.

IR and Raman spectroscopic measurements

IR measurements using the DAC were conducted using an FT-IR microscope (FT/IR4600, IRT-5200, JSACO Co.) equipped with a Ge/KBr beam splitter and liquid N_2-cooled HgCdTe. Absorption spectra were obtained between 800 and 8000 cm^{-1} at a 1.0 or 2.0 cm^{-1} resolution. The reference spectra were measured as the IR light passing through the vacant sample hole of the DAC. The cryostat was placed on an optical rail and moved between the FT-IR and Raman microscopes. This enabled the Raman and IR spectra of the sample to be measured under the same pressure-temperature (P–T) conditions.

The Raman microscope (ST-LV100, AIRIX Co.) consisted of a 532-nm diode-pumped solid-state laser (100 mW), a high-pass filter, and a polychromator (Kymera, Andor Co.). The polychromator was equipped with a charge-coupled device detector having an image resolution of 256 × 2000 pixels (iVac316; Andor Co.). A diffraction grating with 1800 grooves/mm was selected for the Raman and ruby fluorescence measurements. The energy axes of the Raman and ruby-fluorescence spectra were calibrated using neon emission lines. The spectral resolution was approximately 0.7 cm^{-1}. The laser beam was focused on the samples in the DAC through an objective lens at a ×20 magnification (20XLWD, N.A. = 0.30, Nikon Co.).

Results and Discussion

P-T paths

Figure 1 shows the representative P–T path in the ten experimental series. The type I clathrates of MH and EH were cooled to 100 or 10 K while maintaining the pressures below 1 GPa; thereafter, they were isothermally compressed. Changes in the Raman and IR spectra, which indicate the progress of PIA as mentioned in a later section, were observed in the P-T regions shown in **Fig. 1**. To investigate the structural changes in amorphous MH and EH caused by annealing, the samples were annealed at 180 K and 2–6 GPa after PIA for part of the ten experimental series.

The filled-ice structure of MH, which is a stable phase above 1.9 GPa (termed phase III), solid methane, and solid ethane, was also measured at high pressures and low temperatures. Solid methane was produced as a metastable phase by the quick compression of MH at approximately 2 GPa and room temperature,[32] whereas solid ethane was produced by the decomposition of EH at approximately 4 GPa and room temperature.[31,33]

PIA or MH

Figure 2a–c show the Raman spectra of MH under isothermal compression at 100 K. The Raman bands assigned to the phonon modes, which are characteristic to the type I clathrate structure, appeared at 200–400 cm^{-1} below approximately 2 GPa (**Fig. 2a**).[34] Measurement of the phonon mode provides information about the long-range order in the structure. The phonon Raman bands exhibited a blue shift with increasing pressure. No marked changes were observed in the Raman bands below 2 GPa at 100 K, suggesting that no phase transitions occurred. The intensities of the Raman bands gradually decreased with increasing pressure above approximately 2 GPa, and the bands finally disappeared at approximately 3.5 GPa. This implies that the host cage collapsed at 2–3.5 GPa, that is, PIA occurred. This PIA P–T range is consistent with the results of the high-pressure neutron diffraction study for deuterated MH.[14] The neutron diffraction peaks for the crystalline MH disappeared at 3.2 GPa and 100 K, and the split FDP for the amorphous phase appeared.[14] The rate of PIA was inhomogeneous in the sample hole of the DAC, which may suggest that deviatric stress in the sample hole served as a trigger for PIA.

The vibron modes of the guest methane molecules provide information about the local structure around the methane molecules during PIA. Two v_1 Raman bands appeared in the CH stretching region (**Fig. 2b**). The low- and high-wavenumber Raman bands were assigned to the guest methane molecules in the large and small cages, respectively (**Fig. 2c**). The magnitude of the host–guest interactions was larger in the small cage than in the large cage. This assignment is consistent with the "loose cage–tight cage" model.[23,24] In fact, the ratio of the areas of the two Raman bands is proportional to the relative occupancies of the guest methane molecules in the large and small cages.[35] **Figure 3a** shows the peak wavenumbers of the v_1 Raman bands as a function of pressure at 100 K, which were determined by a peak-fitting analysis using a split-Pearson VII function. All v_1 Raman bands exhibited a blue shift at pressures below 2 GPa at 100 K. This indicates that the repulsive host-guest interaction is enhanced by cage shrinkage. The pressure effect on the host-guest interaction within the small cage is large because of the small cavity space around the guest methane molecule, as compared to that in the large cage. Consequently, the pressure shift rate of the v_1 Raman band of the methane molecule in the small cage was higher than that in the large cage (**Fig. 3a**).

The shapes of the v_1 Raman bands changed at 2 GPa, where PIA occurred. Above 2 GPa, the v_1 Raman band of the large cage decreased with increasing pressure, whereas that of the small cage grew and widened with progressing amorphization (**Fig. 2c**). The v_1 Raman band of the large cage disappeared completely at approximately 4 GPa. **Figure 3c** shows the full width at half maximum (FWHM) of the Raman band of the small cage as a function of pressure at 100 K. The FWHM values

increased sharply at 2–4 GPa and subsequently gradually increased above 4 GPa as amorphization progressed. The error bars in **Figs. 3a–c** show the variation in the values depending on the position in the sample hole. This means that the progress of the PIA was sluggish and depended on the deviatoric stress.

The ν_1 Raman bands of solid methane and phase-III also exhibited a single peak, similar to the amorphous MH (**Fig. 2c**). However, their FWHM values were considerably lower than those of amorphous MH (**Fig. 3c**). This indicates that phase separation was not accompanied by PIA. The very short diffusion lengths of water and methane molecules at low temperatures probably prevented the nucleation of phase-III or solid methane. The diffusion coefficient of water molecules in MH at 100 K is estimated to be only approximately 10^{-20} nm^2/s from those of the high-pressure phases of ice.[36,37] Therefore, a regular array of methane molecules was maintained, even in the amorphous form. Therefore, the broad ν_1 Raman band of amorphous MH was caused by methane molecules enclosed in the collapsed cages. The growing ν_1 Raman band of the small cage and the decreasing band of the large cage during PIA indicate that the cavity sizes of all the collapsed cages around the methane molecules were similar to those of the small cages. The large cages shrank with the remaining coordination number around the methane molecule during PIA. This structural model is supported by previous MD studies of amorphous MH and Xe hydrates, which have type I clathrate structures.[14,21]

The peak wavenumbers of the ν_1 Raman band of the small cage decreased in a stretched sigmoid-shaped manner when amorphous MH was depressurized after the maximum pressure was reached (**Fig. 3b**). The hysteresis between the peak wavenumbers before and after PIA was caused by the change in the cavity size caused by PIA. The increase in the peak wavenumber due to PIA (**Fig. 3b**) indicates that the collapsed cages were smaller than the crystalline small cages. This densification of MH by PIA is consistent with the results of previous volumetric studies on other type II clathrate hydrates.[8,9]

Notably, the in intensity of the Raman band from the ν_4 mode, which corresponded to the bending mode of the methane molecules (**Fig. S2**), significantly increased with the progressive amorphization (**Fig. 2a**). An MD study on crystalline MH suggested that changes in the dipole moment and polarizability of the ν_4 mode of the guest methane molecules are relatively small because the bending motion is hindered in the cages.[38] Collapsing cages may remove such spatial restriction for the bending vibrational motion.

Pressure response of collapsed cages

The Raman bands from the OD stretching modes of the cages provide information about the hydrogen bonds between the D_2O molecules (**Fig. 2b**). According to the correlations between the OH stretching frequencies and the OH···O bond distances,[39,40] decreasing the OH stretching frequency means shortening the OH···O bond distances, that is, enhancement of the hydrogen bond. The OD stretching band of the cages did not overlap with that of the ices (I_h, VI, VII', VIII, and IX) coexisting with MH in the sample hole. Furthermore, the wavenumbers were lower than those of the ices. This implies that the hydrogen bonds between D_2O forming the cage structure of MH are stronger than

those of the ices. **Figure 4** shows the peak wavenumbers of the OD stretching band of MH at 100 K as a function of pressure. All the OD stretching bands exhibited a red shift with pressure below 2 GPa at 100 K, indicating enhancement of the hydrogen bonds with pressure.

The OD stretching band of the cages was broadened at 2 GPa by PIA (**Fig. 2b**). This change in the shape of the OD stretching band was very similar to the spectral change during amorphization from ice I_h to HDA.[41] The shape of the broad band may correspond to the wavenumber distribution, that is, the distribution of the hydrogen bond length.[41] The peak wavenumbers increased abruptly as PIA progressed (**Fig. 4**), which indicates that the average OD···O bond distances were elongated despite the densification by PIA. Regarding the decompression behavior after the maximum pressures were reached, it is noteworthy that the peak wavenumber was almost steady at 2–5 GPa (**Fig. 4**). This pressure dependence indicates that the average OD···O bond distance did not change. The radial distribution functions of amorphous MH, which were determined by the neutron diffraction measurement, also show that the average OD···O bond distances were almost incompressible at 3.2–3.9 GPa at 100 K.[14] These results indicate that the compaction of the collapsed cages was induced by folding of the water-networks, that is, bending of the OD···O linkage, not by the shortening intermolecular distances between water molecules. Such a paradoxical relationship between the density and OH···O bond distance has also been observed in HDA and VHDA using X-ray diffraction and Raman spectroscopy.[6,17,42,43] Interestingly, the compression behaviors of amorphous MH and ice are very similar to those of glasses consisting of a network of corner-shared SiO_4 tetrahedra, such as silica and silicate glasses. Their main compression mechanisms are a reduction in the Si-O-Si bond angles and an increase in the Si-O bond distances with pressure.[44–47] Numerous researchers have pointed out the crystallographic analogy between silica and ices,[48,49] and our results imply that the compression mechanisms of their amorphous forms are similar.

The peak wavenumbers of the OD stretching mode of the collapsed cages were significantly lower than those of HDA (2466 cm^{-1} at 1 atm and 77 K) and VHDA (2484 cm^{-1} at 1 atm and 77 K).[17] This means that the OD···O bond distances in the collapsed cages were significantly smaller than those in the amorphous ices. The repulsive interactions between the methane and water molecules in the collapsed cage could induce effective compaction of the water networks in the gaps between the methane molecules.

Rotational dynamics of the guest methane molecule during PIA

The PIA of MH has been observed even under isothermal compression at 10 K. The onset pressure of PIA at 10 K was approximately 3.5 GPa, at which the Raman spectra changed (**Figs. S3a–d**). This value was higher than the onset pressure at 100 K and roughly corresponded to the extrapolated decomposition curve. The IR spectra of the CH stretching region upon isothermal compression at 10 K are shown in **Fig. 5** (full spectrum: **Fig. S4**). Although the absorption of the ν_3 IR band at room temperature was very weak, it significantly increased and split into several peaks below 40 K (**Fig. S5a**). The ν_3 IR bands in the range of 2980–3015 cm^{-1} were assigned to the methane molecule in the large cage, and the two bands in the range of 3015–3040 cm^{-1} were assigned to the methane molecule in the small cage (**Fig. 5**).[25,26] The splitting of the ν_3 IR bands is caused by the

ro-vibrational transition of the methane molecule in the large cage.[25,26] The rotational energy level (J = 0→1) determined using the quasi-inelastic neutron scattering spectra was approximately 8 cm^{-1},[50] which corresponds to the energy interval of the split ν_3 bands of the methane molecule in the large cage. In contrast, the ν_3 bands of the methane molecule in the small cage did not exhibit the ro-vibrational transition. The rotational motion of the methane molecule enclosed in the cramped cage was hindered by the small cavity around the methane molecules. All ν_3 IR bands, including the ro-vibrational bands, exhibited a blue shift at pressures below 2 GPa at 10 K.

The broadening of the IR bands above 2 GPa is remarkable. This may be due to the deviatoric stress in the sample hole of the DAC or the precursor phenomena of PIA. The splitting caused by the ro-vibrational transition at 3.6 GPa could not be distinguished by the broadening (**Fig. 5**). In the IR spectra of MH, intense absorption bands assigned to the OH stretching modes of the H_2O cage appeared at 2900–3500 cm^{-1}, which has a negative pressure dependence caused by enhancement of the hydrogen bond. Furthermore, the absorption band of the OH stretching mode overlapped with and hindered the identification of the triply degenerate ν_3 modes at approximately 3000 cm^{-1}.

After PIA, the ν_3 IR bands measured when the pressure was decreased to 1.5 GPa at 10 K exhibited a broad single peak (topmost spectrum in **Fig. 5**). This indicates that the rotational motion of the methane molecule in the large cage was frozen by the PIA. An MD study also suggested that its rotational motion becomes 2.5–3-fold slower than the almost-free rotation in crystalline MH.[22] Furthermore, freezing of the rotational motion of the guest molecules by PIA was also observed in THF hydrate. The results of a dielectric spectroscopic study on THF hydrate demonstrated that the high-frequency permittivity due to the rotational motion of THF molecules in the very large ($5^{12}6^4$) cages decreased slightly during PIA.[16] An MD study on amorphous THF hydrate also supported the freezing rotational motion.[18] These results suggest that the cavity spaces around the guest molecules in the large cages shrink by collapsing, restricting the rotational motions.

PIA of EH

The Raman and IR spectra of EH under isothermal compression at 100 K are shown in **Figs. 6a–d** and **S6**, respectively. The Raman and IR bands in the C-H stretching wavenumber region widened above 4 GPa, which is typical of PIA (**Figs. 6b** and **S6**). It is currently difficult to assign normal modes to the Raman and IR bands. There are only two Raman active C-H stretching normal modes of the ethane molecule, namely, ν_1 and ν_{10} (**Fig. S2**). However, at least seven peaks appeared in the C-H stretching wavenumber region at low temperatures (**Fig. 6b**). These peaks can be attributed to many candidates such as overtone modes (for example, $2\nu_8$) and splitting of the ν_1 and ν_{10} modes due to differences of the host-guest interaction in the small and large cages. The assignment of the Raman bands of EH in the C-H stretching wavenumber region in previous studies is inconsistent.[33,51] A well-grounded assignment of the IR spectra of the C-H stretching wavenumber regions was difficult. Further studies are needed to determine the CH stretching Raman and IR bands of EH. The shapes of the Raman and IR bands were clearly different from those of solid ethane (**Figs. 6b** and **S6**). This indicates that phase separation did not occur. The Raman bands of the ν_3 and bending (ν_{11}) modes of the guest ethane molecule (**Fig. S2**), in contrast, had very simple

shapes (**Figs. 6c** and **d**) and provided information about the local structure around the guest ethane molecules after PIA. The v_{11} Raman bands were very weak and ambiguous at room temperature and grew in intensity with decreasing temperature. Both the v_3 and v_{11} modes were split into two Raman bands due to the difference in the magnitude of the host–guest interaction in the large and small cages (**Figs. 6c** and **d**). Their low- and high-wavenumber Raman bands were assigned to guest ethane molecules in the large and small cages, respectively,[33,51] in a similar manner to the v_1 Raman bands of MH. The ratio of the areas of the two Raman bands shows that the occupancy of the small cage was not as high as that of the large cage.[33] In the case that both cages are fully occupied, the ratio of the areas would be large cage: small cage = 3:1. A previous Raman spectroscopy study on methane-ethane mixed hydrates suggested that guest ethane molecules preferentially occupy large cages.[33] This preferential cage occupancy is attributed to the large repulsive interaction between the ethane and water molecules in the small cage. All v_3 and v_{11} Raman bands showed a pressure blue shift below 4 GPa without changing of the band shapes (**Figs. 6c** and **d**). The pressure-shift rates of the Raman bands from the ethane molecule in the small cage were higher than those in the large cage (**Figs. 7a** and **c**).

Above 4 GPa, the v_3 and v_{11} Raman bands of the large cage widened with progressing amorphization (**Figs. 6c** and **d**). **Figures 7b** and **d** show the FWHM values of the Raman bands of the large cage as a function of pressure. The FWHM values increased sharply at 4–5 GPa, and then gradually increased above 5 GPa. In contrast, the intensities of the v_3 and v_{11} Raman bands of the small cage decreased with progressing amorphization. Such selective growth and reduction of the v_3 and v_{11} Raman bands during PIA indicate that all collapsed cages containing ethane molecules were similar to the large cage. The small cages, containing the ethane molecules, expand to the size of the large cages during PIA by collapsing. This is in contrast with amorphous MH, which has a small cage-like structure.

The v_3 and v_{11} Raman bands of the small cage disappeared completely at approximately 5.5 GPa, where EH was completely amorphized. The collapse pressure (onset and completion; 4–5.5 GPa at 100 K) of EH was higher than that for MH (2–3.5 GPa at 100 K). The decomposition curves of both hydrates had negative slopes, and the decomposition pressures of MH and EH at room temperature were approximately 2 and 4 GPa, respectively (**Fig. 1**). Extrapolation of their curves to low temperatures roughly corresponded to the P-T conditions where PIA occurred. One explanation for the difference of the collapse pressure may be that the size of the guest molecules affects the mechanical stability. Here, it is noteworthy that our samples were synthesized from D_2O and the isotope substitution may affect slightly the stability.

The pressure dependences of the peak wavenumbers of the v_3 and v_{11} Raman bands of the large cage exhibited irreversible change upon decompression after PIA (**Figs. 7a** and **c**). The peak wavenumbers decreased in a sigmoidal manner when the amorphous EH was depressurized after the maximum pressure was reached. This hysteresis behavior suggests that the cavity sizes of the collapsed cages were smaller than those of the large crystalline cages.

The IR spectra of EH was also obtained at 10 K before and after PIA (**Fig. S5b**). Ro-vibrational transitions were not observed in the IR spectra of the crystalline and amorphous EH, as reported in a previous study.[52] This is in contrast to the rotational dynamics of the methane molecule in the

large cage of crystalline MH (**Fig. 5**). The differences in the rotational dynamics of the guest molecules in crystalline MH and EH may be caused by the free cavity volume, where the guest molecules can rotate freely. The ratios of the van der Waals volume of methane molecules to the cavity volumes in the small and large cages of MH were estimated to be 27 and 19 vol%, respectively, whereas those of EH were 55 and 39 vol%, respectively.[53] The threshold value of the ro-vibrational transition was approximately 20 vol%.

Differences in the structure between amorphous MH and EH

During the isothermal compression of EH at 100 K, the Raman band from the OD stretching modes of the cages was broadened by PIA at 4 GPa (**Fig. 6b**). **Figure 4** shows the peak wavenumbers of the OD stretching band of EH at 100 K as a function of pressure. Although the peak wavenumber of amorphous EH changed with pressure in a manner similar to that of amorphous MH, it was approximately 100 cm^{-1} lower than that of amorphous MH. This suggests that the compression mechanisms of amorphous EH and MH were similar, whereas the hydrogen bonds in the former were stronger than those in the latter. The average OD···O bond distance in the collapsed cages of amorphous EH was estimated to be approximately 0.1 Å shorter than that of amorphous MH from the correlations between OD stretching frequencies and the distances.[40] The correlation between the van der Waals radii of the methane and ethane molecules and the OD stretching frequencies of their amorphous hydrates (average OD···O bond distance) are shown in **Fig. 8**. Interestingly, in the case where the size of the guest molecule in the amorphous ices (LDA, HDA, and VHDA), including the amorphous ices in **Fig. 8**, is assumed to be "zero," a linear relationship exists in the dataset.[17] This implies that the guest molecules play the role of a "molecular filler" in the amorphous clathrate structure.[11] The water networks in the gap between the homogeneously distributed guest molecules were densified depending on the size of the guest molecules.

Annealing effect on amorphous MH and EH

Amorphous MH and EH formed by compression at 100 K were annealed at 180 K, which exceeds the glass transition temperature of HDA (130 K),[20] and 2.5–3.0 GPa and 5.5–6.1 GPa, respectively, for 8–10 h. **Figure 9** shows the Raman spectra of amorphous MH and EH during annealing. The spectral features did not change with annealing significantly, and phase separation did not occur. Subsequently, the annealed amorphous MH and EH were cooled to 100 K, and their IR and Raman spectra were measured. No significant changes were observed in the pre- and post-annealing spectra, as shown in **Fig. 9**. However, the FWHM values of the vibron Raman bands, the ν_1 Raman bands of the amorphous MH (**Fig. 3c**) and the ν_3 and ν_{11} Raman bands of the amorphous EH (**Fig. 7b** and **d**), were slightly decreased by annealing. This means that the distributions of the vibrational states of the methane and ethane molecules narrowed. The peak wavenumbers of the OD stretching modes of the amorphous MH and EH did not change upon annealing (**Fig. 4**), whereas those of the vibron modes decreased (**Figs. 3b, 7a** and **c**). In particular, the wavenumbers of the ν_3 and ν_{11} modes of amorphous EH were approximately 10 cm^{-1} lower than those before annealing. This implies that the average distances between the methane or ethane molecules and water molecules were elongated.

The structures around the methane and ethane molecules were relaxed by releasing frustration due to repulsive host-guest interactions. Previous neutron diffraction measurements indicate that annealing rearranges and densifies the water networks in amorphous clathrate hydrates,[14,18,21] whereas our results show that the local structure around the guest molecules becomes less dense by annealing. Although it is not certain whether such structural changes correspond to a polyamorphic transition, such as the transition from HDA to VHDA, the strained amorphous clathrate hydrates must be equilibrated using annealing.

Conclusions

The results of this study depict the structure and dynamics of amorphous type I clathrate hydrates as follows: the cages collapsed by PIA without any reconstruction of the water networks or diffusion of guest molecules. Consequently, the cavity remained even after PIA owing to the repulsive interaction between the guest and water molecules. Therefore, the medium-range structure must be characterized by a cage-like structure. The cavity sizes of the cages became compatible with the sizes of the guest molecules upon collapse. The rotational motion of the guest molecules in the collapsed cage was frozen for spatial restriction. The water network around a larger guest molecule, such as ethane, was tightly compacted by its strong repulsive host-guest interactions when PIA occurred. Further research is required to understand the continuous relationship between the average OH···O bond distance in the collapsed cage and the sizes of guest molecules (**Fig. 8**). To verify this relationship, the PIA structures of various amorphous clathrate hydrates, including other guest molecules and type II clathrates, should be investigated using vibrational spectroscopy and neutron diffraction measurements.

Conflicts of interest

There are no conflicts to declare.

Acknowledgements

N.N. would like to thank Dr. A. Tani of Kobe University for his useful advice concerning the synthesis of methane hydrate and Dr. Y. Ohno of Tokushima University for his technical advice on Raman spectroscopy. This study was financially supported by Grant-in-Aids (Nos. 17K14422, 17H06456, and 20K04131) from the Japan Society for Promotion of Science.

References

1 P. Gallo, K. Amann-Winkel, C. A. Angell, C. M. A. Anisimov, F. Caupin, C. Chakravarty, E. Lascaris, T. Loerting, A. Z. Panagiotopoulos, J. Russo, J. A. Sellberg, H. E. Stanley, H. Tanaka, C. Vega, L. M. Xu, L. G. M. Pettersson, *Chem. Rev.*, 2016, **116**, 7463–7500.

2 H. E. Stanley, S. V. Buldyrev, M. Canpolat, O. Mishima, M. R. Sadr-Lahijany, A. Scala and F. W. Starr, *Phys. Chem. Chem. Phys.*, 2000, **2**, 1551–1558.

3 O. Mishima, L. D. Calvert and E. Whalley, *Nature*, 1984, **310**, 393–395.
4 O. Mishima, L. D. Calvert and E. Whalley, *Nature*, 1985, **314**, 76–78.
5 T. Loerting, C. G. Salzmann, I. Kohl, E. Mayer and A. Hallbrucker, *Phys. Chem. Chem. Phys.*, 2001, **3**, 5355–5357.
6 M. Guthrie, C. A. Tulk, C. J. Benmore and D. D. Klug, *Chem. Phys. Lett.*, 2004, **397**, 335–339.
7 J. L. Finney, A. Hallbrucker, I. Kohl, A. K. Soper and D. T. Bowron, *Phys. Rev. Lett.*, 2002, **88**, 225503–1–4.
8 R. G. Ross and P. Andersson, *Can. J. Chem.*, 1982, **60**, 881–892.
9 Y. P. Handa, J. S. Tse, D. D. Klug and E. Whalley, *J. Chem. Phys.*, 1991, **94**, 623–627.
10 Y. Suzuki, Phys. Rev. B: Condens. Matter Mater. Phys., 2004, **70**, 1–4.
11 O. Andersson and A. Inaba, *J. Phys. Chem. Lett.*, 2012, **3**, 1951–1955.
12 O. Andersson and U. Häussermann, *J. Phys. Chem. B*, 2018, **122**, 4376–4384.
13 P. H. B. Brant Carvalho, A. Mace, O. Andersson, C. A. Tulk, J. Molaison, A. P. Lyubartsev, I. M. Nangoi, A. A. Leitão and U. Häussermann, *Phys. Rev. B: Condens. Matter Mater. Phys.* 2021, **103**, 064205–1–11.
14 C. A. Tulk, D. D. Klug, J. J. Molaison, A. M. Dos Santos and N. Pradhan, *Phys. Rev. B: Condens. Matter Mater. Phys.*, 2012, **86**, 1–8.
15 O. Andersson and Y. Nakazawa, *J. Phys. Chem. B*, 2015, **119**, 3846–3853.
16 O. Andersson and G. P. Johari, *J. Chem. Phys.*, 2008, **129**, 234505.
17 T. Loerting, K. Winkel, M. Seidl, M. Bauer, C. Mitterdorfer, P. H. Handle, C. G. Salzmann, E. Mayer, J. L. Finney and D. T. Bowron, *Phys. Chem. Chem. Phys.*, 2011, **13**, 8783–8794.
18 P. H. B. Brant Carvalho, A. Mace, C. L. Bull, N. P. Funnell, O. Andersson and U. Häussermann, *J. Chem. Phys.*, 2019, **150**, 204506.
19 O. Andersson, P. H. B. Brant Carvalho, U. Häussermann and Y. J. Hsu, *Phys. Chem. Chem. Phys.*, 2022, **24**, 20064–20072.
20 T. Loerting, V. F. Landete, P. H. Handle, M. Seidl, K. A. Winkel, C. Gainaru and R. Böhmer, *J. Non-Cryst. Solid.*, 2015, **407**, 423–430.
21 P. H. B. Brant Carvalho, P. I. R. Moraes, A. A. Leitão, O. Andersson, C. A. Tulk, J. Molaison, A. P. Lyubartsev, U. Häussermann, *RSC Adv.*, 2021, **11**, 30744–30754.
22 N. J. English and J. S. Tse, *Phys. Rev. B: Condens. Matter Mater. Phys.*, 2012, **86**, 104109.
23 G. C. Pimental and S. W. Charles, *Pure Appl. Chem.*, 1963, **7**, 111–124.
24 S. Subramanian and E. D. Sloan, *J. Phys. Chem. B*, 2002, **106**, 4348–4355.
25 E. Dartois and D. Deboffle, *Astron. Astrophys.*, 2008, **490**, L19–L22.
26 N. Noguchi, T. Yonezawa, Y. Yokoi, T. Tokunaga, T. Moriwaki, Y. Ikemoto and H. Okamura, *J. Phys. Chem. C*, 2021, **125**, 189–200.
27 E. D. Sloan, Clathrate Hydrates of Natural Gas, Dekker, New York, 2nd edn, 1998.
28 H. K. Mao, P. M. Bell, J. W. Shaner and D. J. Steinberg, *J. Appl. Phys.,* 1978, **49**, 3276–3283.
29 Y. A. Dyadin, *Mendeleev Commun.*, 1997, **7**, 34–35.
30 A. Kurnosov, L. Dubrovinsky, A. Kuznetsov and V. Dmitriev, *Z. Naturforsch., B: J. Chem. Sci.,* 2006, **61**, 1573–1576.

31 A. V. Kurnosov, A. G. Ogienko, S. V. Goryainov, E. G. Larionov, A. Y. Manakov, A. Y. Lihacheva, E. Y. Aladko, F. V. Zhurko, V. I. Voronin, I. F. Berger and A. I. Ancharov, *J. Phys. Chem. B*, 2006, **110**, 21788–21792.

32 T. Ohtani, Y. Ohno, S. Sasaki, T. Kume, H. Shimizu, *J. Phys. Conf. Ser.*, 2010, **215**, 12051–12058.

33 H. Hirai, N. Takahara, T. Kawamura, Y. Yamamoto and T. Yagi, *J. Chem. Phys.*, 2008, **129**, 224503.

34 S. Sasaki and H. Shimizu, *Low Temp. Sci.*, 2005, **64**, 199–214.

35 A. K. Sum, R. C. Burruss and E. D. Sloan, *J. Phys. Chem. B*, 1997, **101**, 7371–7377.

36 N. Noguchi and T. Okuchi, *J. Chem. Phys.*, 2016, **144**, 234503.

37 N. Noguchi and T. Okuchi, *Icarus*, 2020, **335**, 113401.

38 H. C. Wang, X. L. Zhu, J. W. Cao, X. L. Qin, Y. C. Yang, T. X. Niu, Y. B. Lu and P. Zhang, *New J. Phys.*, 2020, **22**, 093066.

39 K. Nakamoto, M. Margoshes and R. E. Rundle, *J. Am. Chem. Soc.*, 1955, **77**, 6480–6486.

40 W. Mikenda, *J. Mol. Struct.*, 1986, **147**, 1–15.

41 C. A. Tulk, D. D. Klug, R. Branderhorst, P. Sharpe and J. A. Ripmeester, *J. Chem. Phys.*, 1998, **109**, 8478–8484.

42 D. D. Klug, O. Mishima and E. Whalley, *J. Chem. Phys.*, 1987, **86**, 5323–5328.

43 C. G. Salzmann, T. Loerting, S. Klotz, P. W. Mirwald, A. Hallbrucker and E. Mayer, *Phys. Chem. Chem. Phys.*, 2006, **8**, 386–397.

44 G. V. Gibbs, *Am. Mineral.*, 1982, **67**, 421–450.

45 C. Meade, R. J. Hemley and H. K. Mao, *Phys. Rev. Lett.*, 1992, **69**, 1387–1390.

46 Y. Wang, T. Sakamaki, L. B. Skinner, Z. Jing, T. Yu, Y. Kono, C. Park, G. Shen, G. M. L. Rivers and S. R. Sutton, *Nature Comm.*, 2014, **5**, 3241.

47 T. Ohashi, T. Sakamki, K. Funakoshi and A. Suzuki, *J. Min. Petrol. Sci.*, 2018, **113**, 286–292.

48 J. S. Tse, D. D. Klug, J. A. Ripmeester, S. Desgreniers and K. Lagarec, *Nature*, 1994, **369**, 724–727.

49 G. A. Tribello, B. Slater, M. A. Zwijnenburg and R. G. Bell, *Phys. Chem. Chem. Phys.*, 2010, **12**, 8597–8606.

50 J. S. Tse, C. I. Ratcliffe, B. M. Powell, V. F. Sears and Y. P. Handa, *J. Phys. Chem. A,* 1997, **101**, 4491–4495.

51 K. Morita, S. Nakano and K. Ohgaki, *Fluid Phase Equilib.*, 2000, **169**, 167–175.

52 E. Dartois and F. Langlet, *Icarus*, 2021, **357**, 114255.

53 E. D. Sloan and C. Koh, *Clathrate Hydrates of Natural Gases*, CRC Press/Taylor & Francis, Florida, 2007.

Fig. 1 Representative experimental P–T path for MH (green line, Run #1). The black and red solid lines show the decomposition curves of MH [29,30] and EH [31], respectively. The blue and red shaded areas show the stability regions of MH (type I clathrate structure, sI) and EH, respectively. The green and yellow bands indicate the pressures where PIA of MH and EH occurred on the isothermal compressions, respectively.

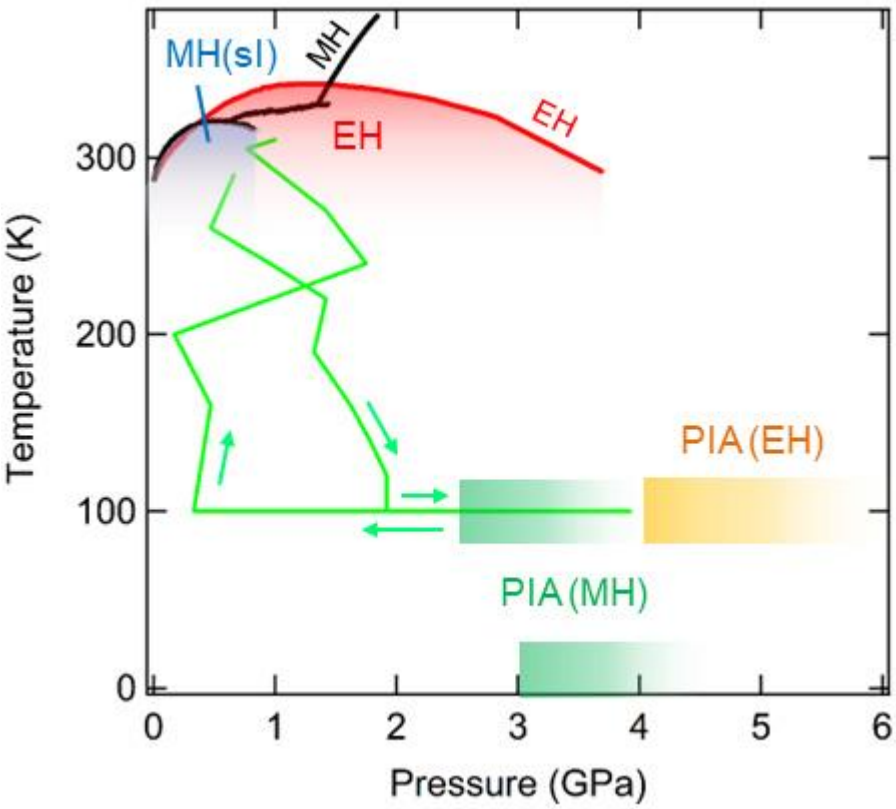

Fig. 2 Raman spectra of MH on the isothermal compression at 100 K. (a) Selected spectra of the phonon/intermolecular mode and CH bending (v_4) modes of the methane molecule. The spectra of ice IX coexisting with MH in the sample hole, solid methane, and phase III of MH are also shown. Strong first-order Raman bands of diamond can be seen at 1200–1400 cm^{-1}. (b) Selected spectra of the OD and CH stretching (v_1, v_3) modes. The bottom spectrum is the Raman spectrum of the diamond anvil, which was measured by focusing the laser beam on the gasket. Weak second-order Raman bands of diamond can be seen at 2200–2700 cm^{-1}. The OD stretching bands of MH are marked with reverse triangles. (c) Magnified view around the v_1 mode. The v_1 band of the methane molecule in the large cage (marked "L") is asymmetrically broadened towards the low-wavenumber side. The asymmetric broadening is caused by comatic aberration in the spectrometer.

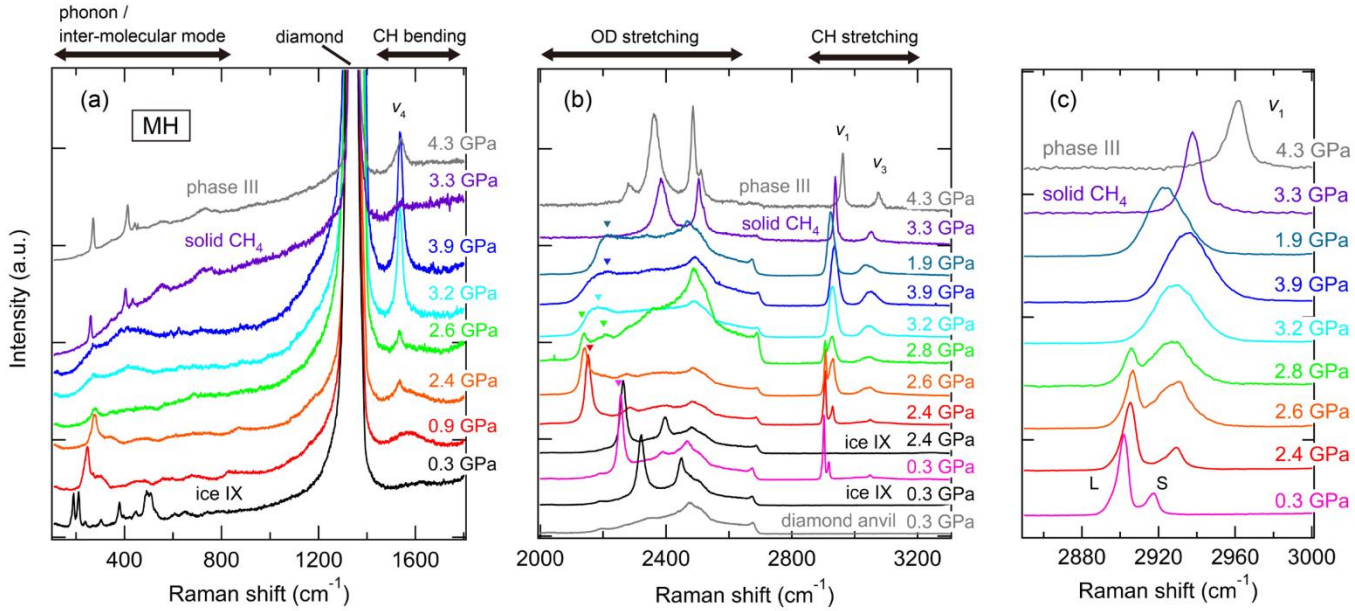

Fig. 3 Peak wavenumbers (a, b) and FWHM (c) of the ν_1 Raman bands of MH and solid methane as a function of pressure at 100 K. The region enclosed by the solid line in (a) is shown in (b). Filled and open symbols show data before and after annealing, respectively. Error bars in each graph indicate the variation in the values depending on the position in the sample hole.

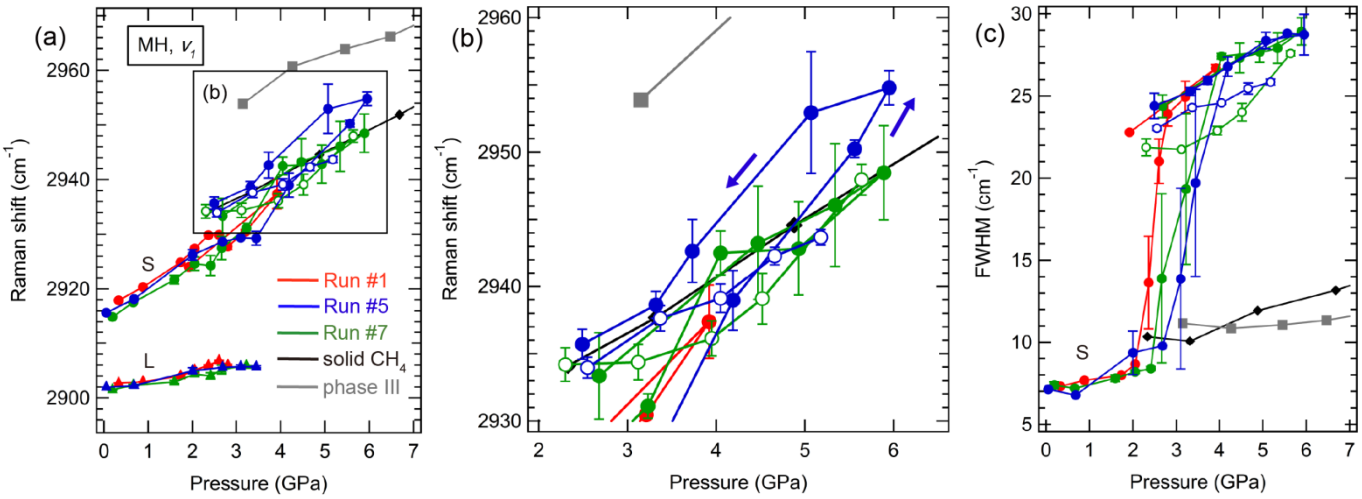

Fig. 4 Peak wavenumbers as a function of pressure for the OD stretching bands of MH, EH, and ices (I_h, VI) at 100 K. Filled and open symbols show data before and after annealing, respectively.

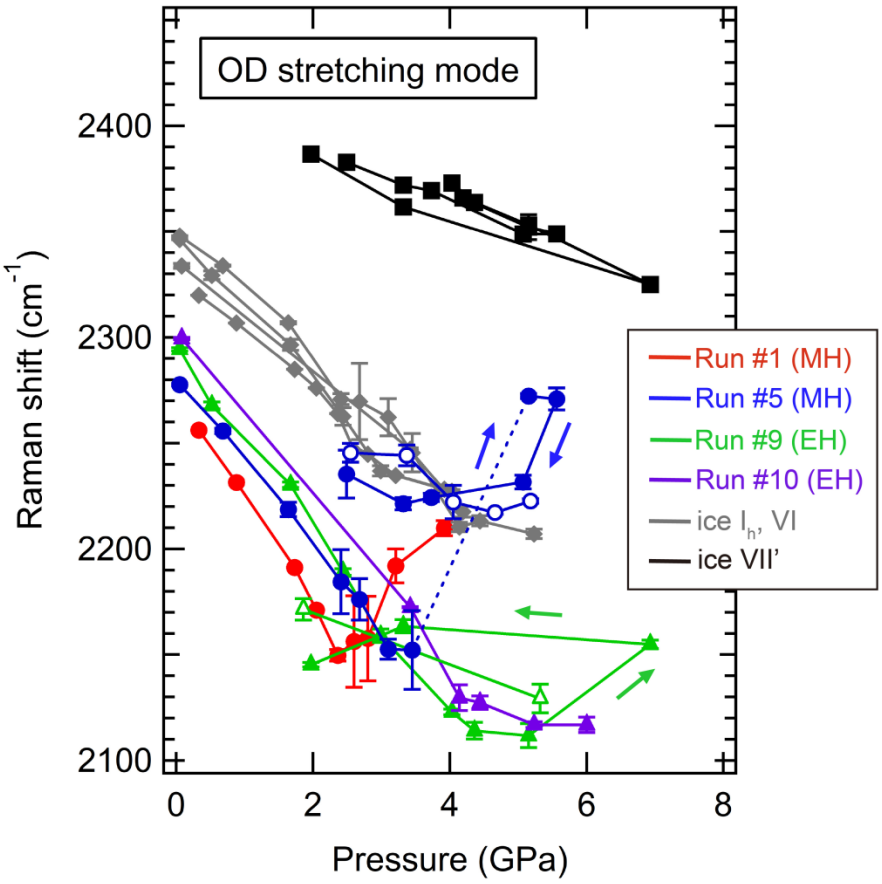

Fig. 5 IR spectra showing v_3 mode of MH on the isothermal compression at 10 K. The assignment of ro-vibrational IR bands (P(2), P(1), Q(1), and R(0)) is based on references [25,26].

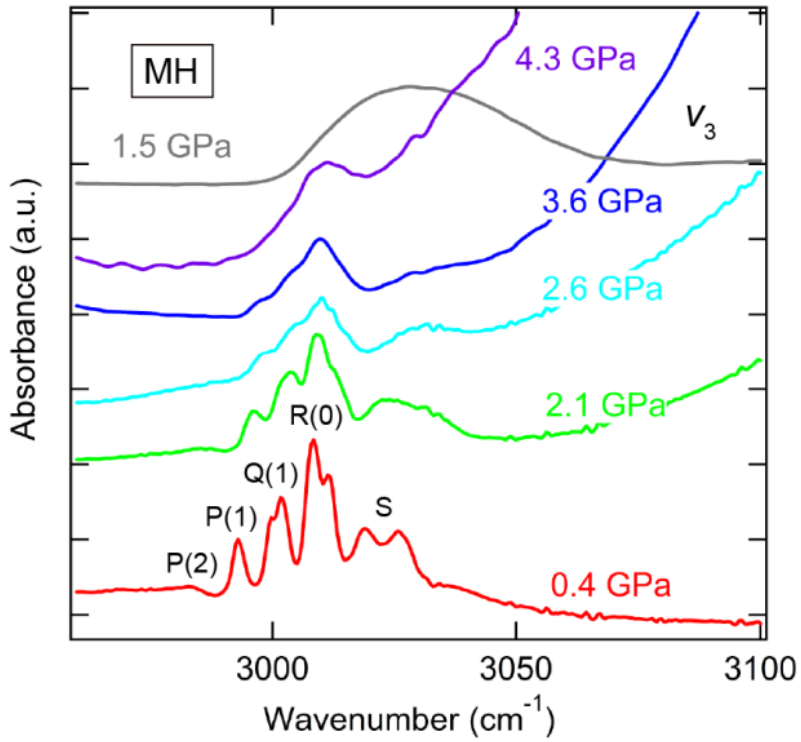

Fig. 6 Raman spectra of EH on the isothermal compression at 100 K. The spectra of ices (I_h, VII') coexisting with MH in the sample and solid ethane are also shown. (a) Selected spectra of the phonon/intermolecular mode, CC stretching (ν_3), and CH bending (ν_{11}) modes of the ethane molecule. (b) Selected spectra of the OD and CH stretching modes. The OD stretching bands of EH are marked with reverse triangles. (c, d) Magnified views around the ν_3 and ν_{11} modes.

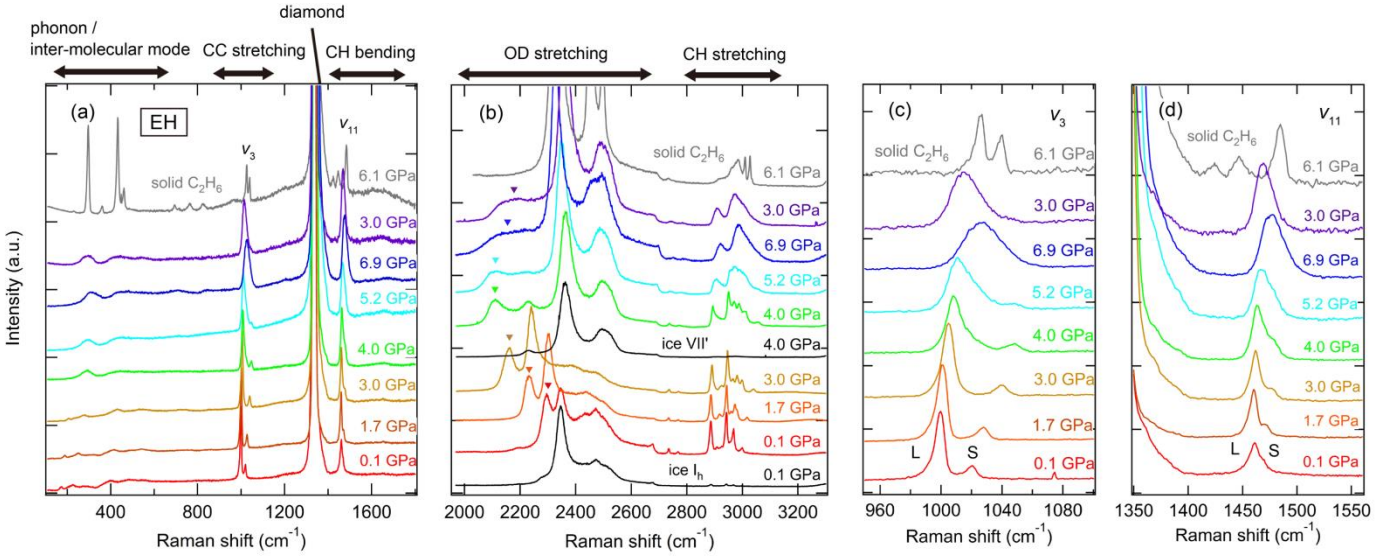

Fig. 7 Peak wavenumbers (a, c) and FWHM (b, d) of the ν_3 and ν_{11} Raman bands of EH as a function of pressure at 100 K. Filled and open symbols show data before and after annealing, respectively.

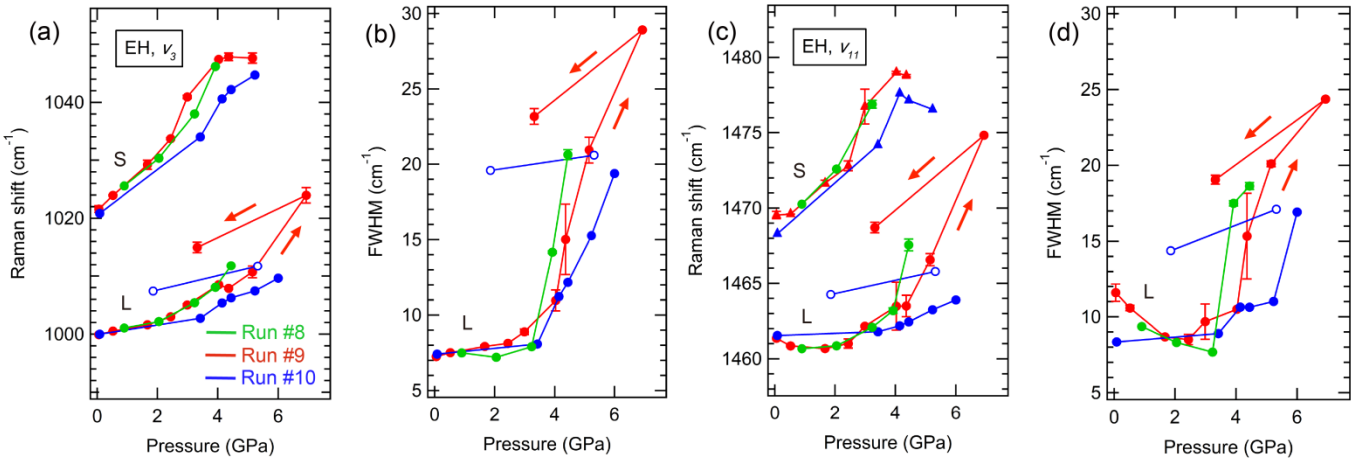

Fig. 8 Correlation between the van der Waals radii of the guest molecules and the OD stretching frequencies of the amorphous hydrates. The frequencies of the OD stretching modes of MH and EH are the average values in the pressure range of 2–7 GPa at 100 K after PIA (**Fig.** 4). Lines are inserted as eye guides for the pre- and post-annealing data (black line: before annealing, red line: after annealing).

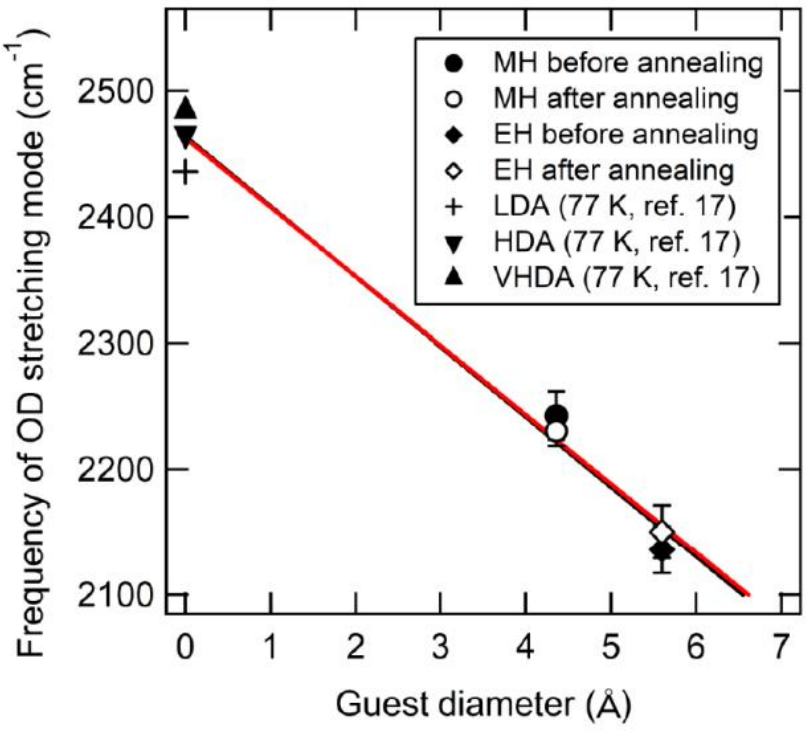

Fig. 9 Raman spectra of the amorphous MH and EH before, during, and after annealing. (a) Selected spectra of the amorphous MH. (b, c, d) Selected spectra of the amorphous EH. The OD stretching bands of MH and EH are marked with reverse triangles.

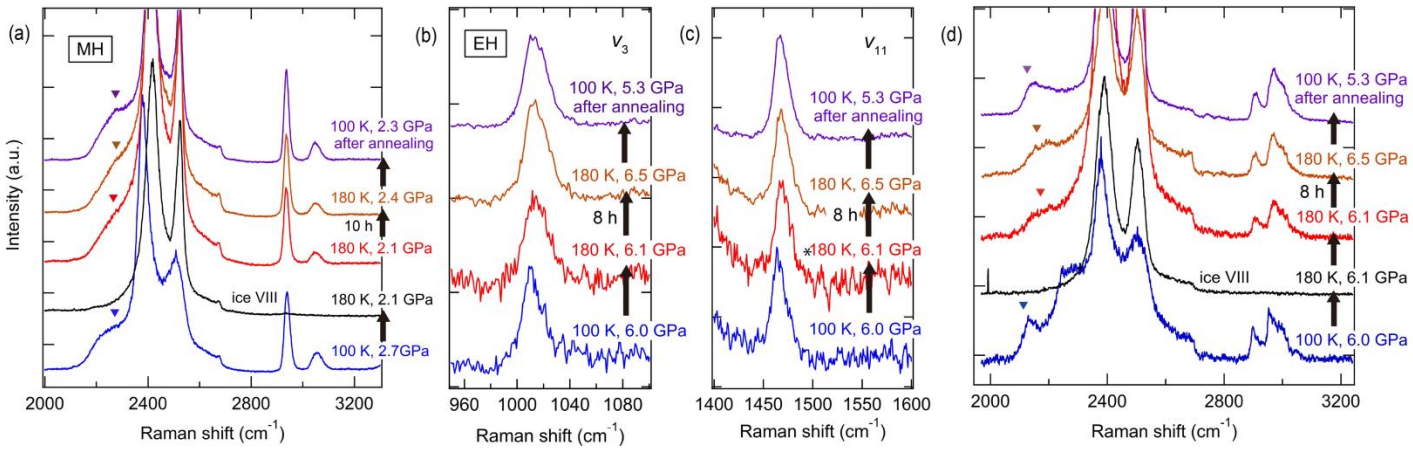

Electronic Supplementary Material (ESI) for Physical Chemistry Chemical Physics.

Supplementary information

Direct observation of pressure-induced amorphization of methane/ethane hydrates using Raman and infrared spectroscopy

Naoki Noguchi,[a]* Yui Shiraishi,[a] Maho Kageyama,[a] Yuu Yokoi,[a] Saki Kurohama,[a] Natsuki Okada,[a] and Hidekazu Okamura[a]

[a] *Graduate School of Technology, Industrial and Social Sciences, Tokushima University, 2-1 Minami-josanjima-cho, Tokushima 770-8506, Japan*

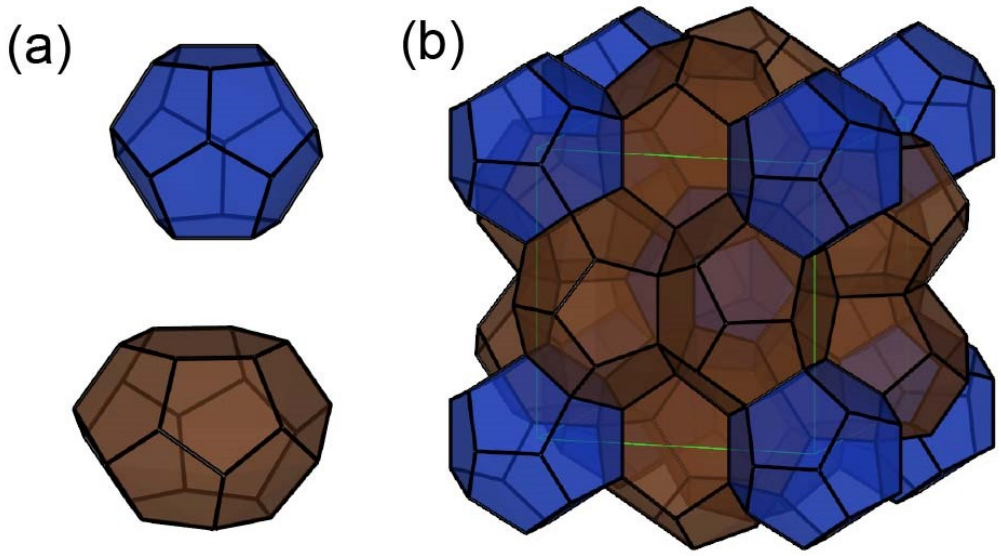

Fig. S1 Crystal structure of the type I clathrate hydrate.[S1] (a) Two cages in the type I clathrate hydrate: small (pentagonal dodecahedron, 5^{12}) cage (blue) and large (tetrakaidecahedron, $5^{12}6^2$) cage (brown). (b) Unit cell composed of two small cages and six large cages.

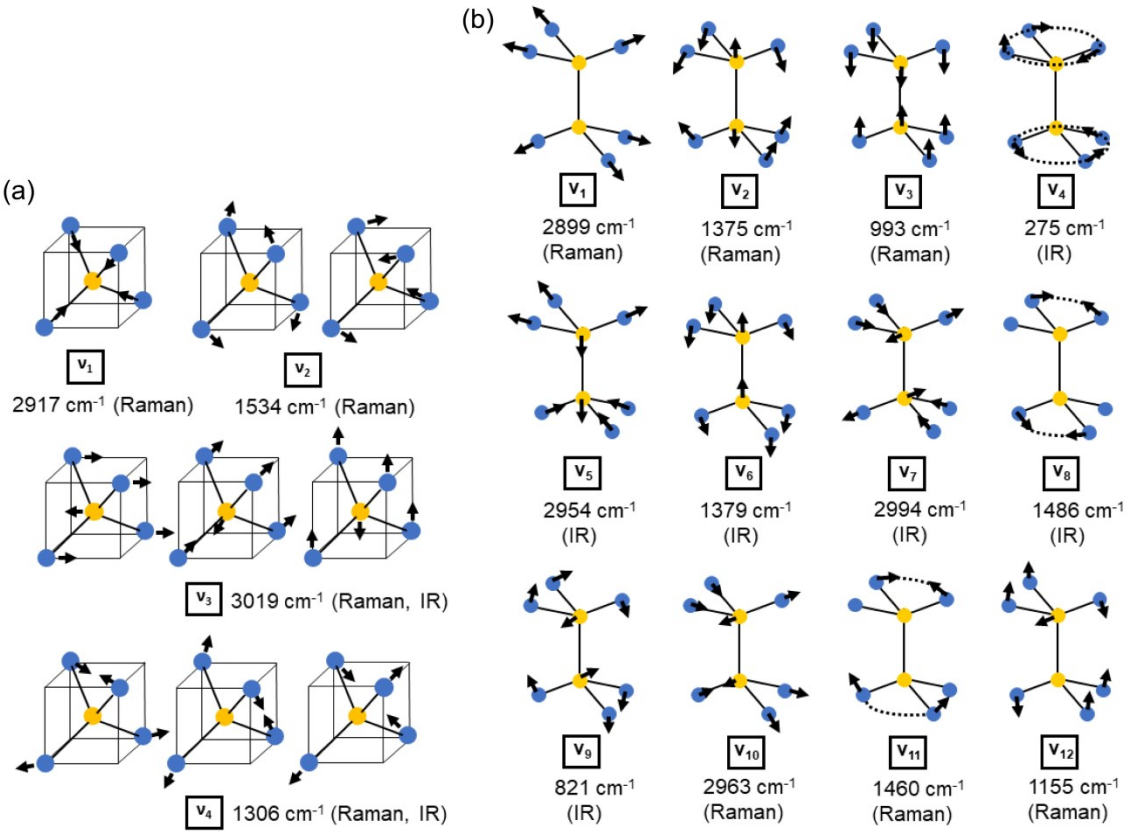

Fig. S2 Normal modes of the methane (a) and ethane molecules (b). The frequencies for the free molecules and Raman and IR activity are shown.[S2] In the figures "Raman" and "IR" indicate Raman and IR activity, respectively.

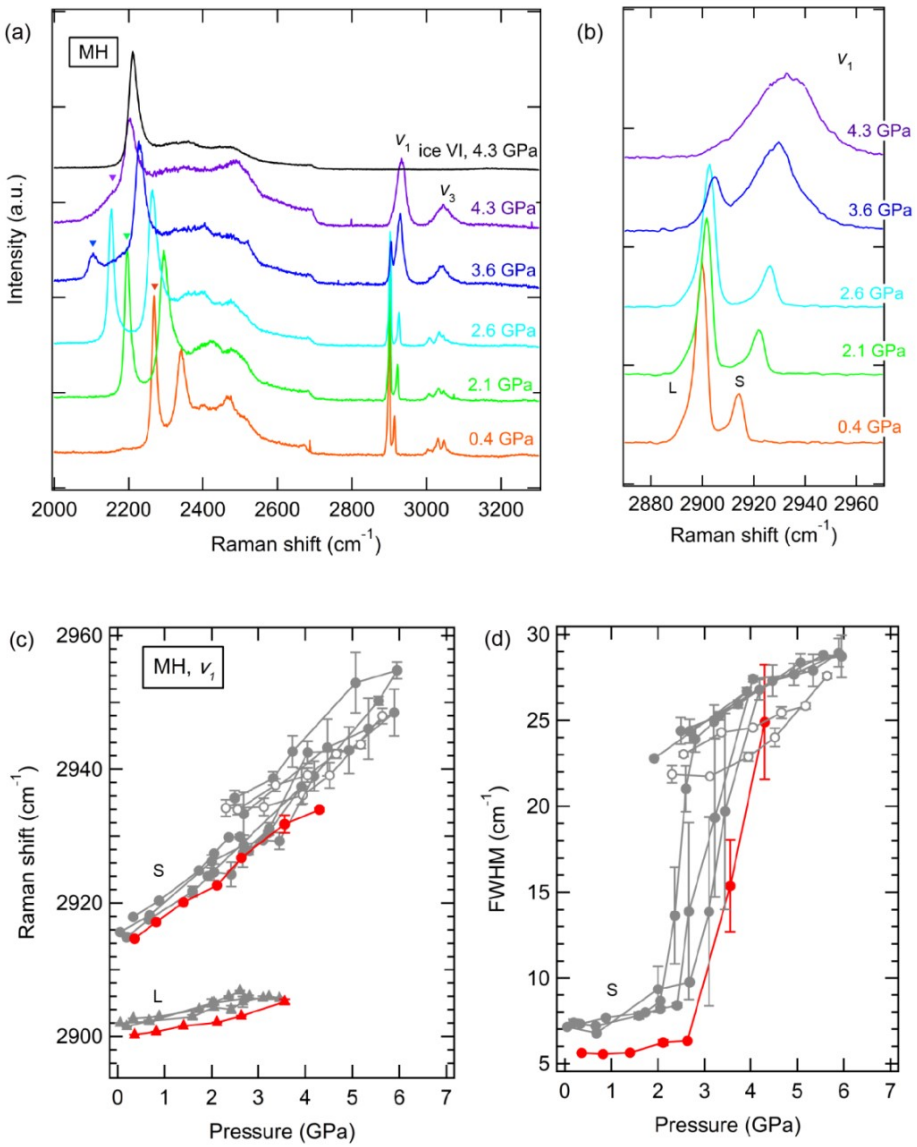

Fig. S3 Raman spectra of MH on the isothermal compression at 10 K. (a) Selected spectra of the OD and CH stretching (ν_1, ν_3) modes. The OD stretching bands of MH are marked with reverse triangles. (b) Magnified view around the ν_1 mode. (c) Peak wavenumbers of the ν_1 Raman bands as a function of pressure at 10 K. (d) FWHM of the ν_1 Raman bands of the methane molecule in the small cage as a function of pressure at 10 K. In (c) and (d), gray points show the dataset at 100 K (Fig. 3).

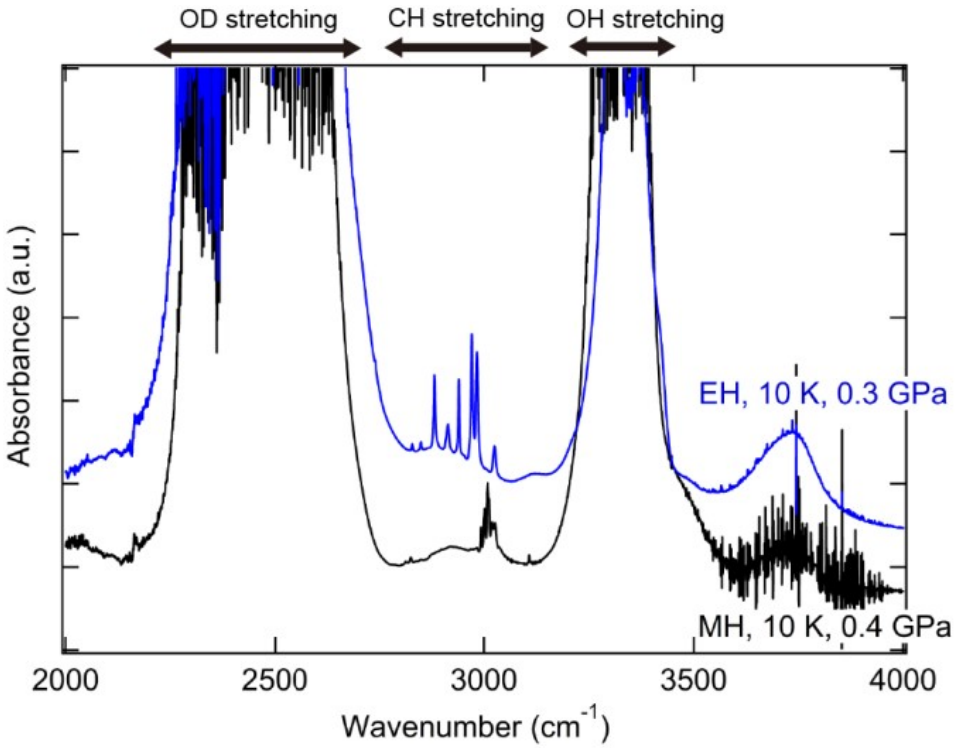

Fig. S4 IR spectra of MH and EH at 2000–4000 cm^{-1}.

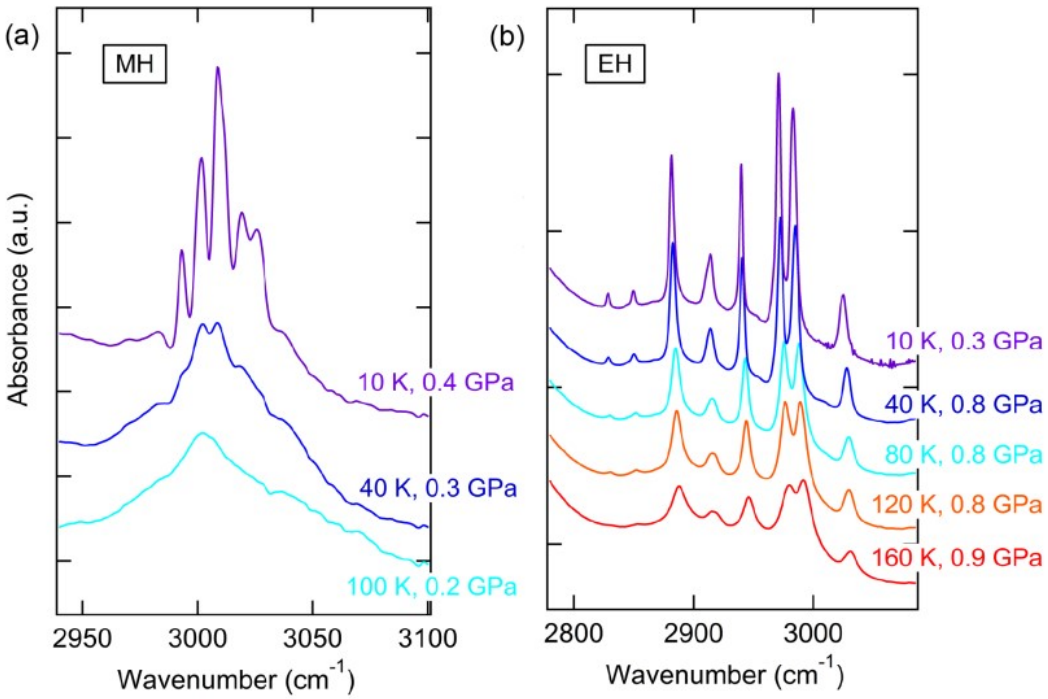

Fig. S5 IR spectra of the CH stretching modes of MH (a) and EH (b) on cooling.

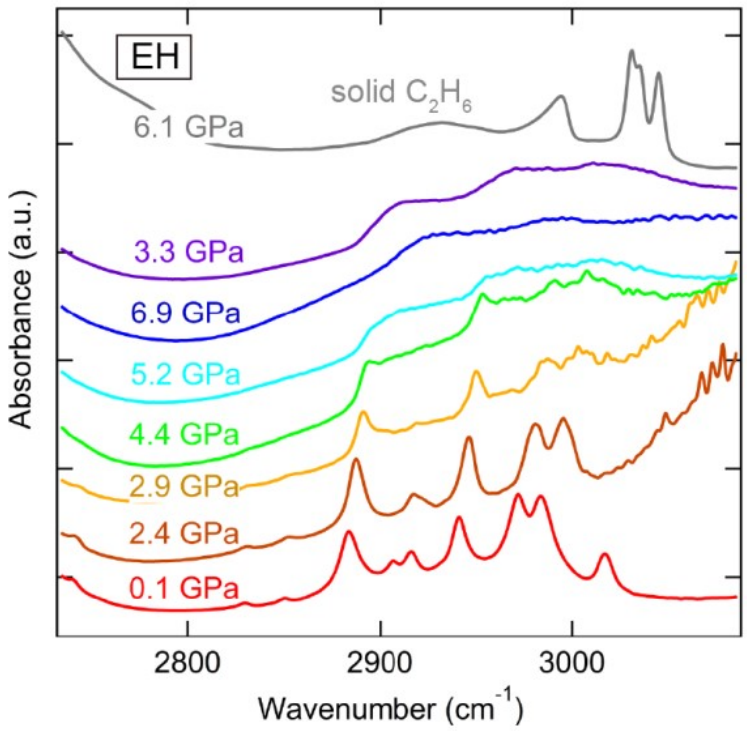

Fig. S6 IR spectra showing the CH stretching mode of EH on the isothermal compression at 100 K. The spectrum of solid ethane is also shown.

References

S1 K. Momma and F. Izumi, *J. Appl. Crystallogr.*, 2011, **44**, 1272–1276.

S2 K. Nakamoto, *Infrared and Raman Spectra of Inorganic and Coordination Compounds,*

Part A: Theory and Applications in Inorganic Chemistry, John Wiley & Sons, New Jersey, 2009.